Investigating cerium redox changes between aluminosilicate glass and melt, a multispectroscopic approach

Adrien Donatini, Peggy Georges, Tiphaine Fevre, Laurent Cormier, Daniel Neuville

Investigating cerium redox changes between aluminosilicate glass and melt, a multispectroscopic approach.

Adrien Donatini[a,b,c], Peggy Georges[a], Tiphaine Fevre[a], Laurent Cormier[b], Daniel R. Neuville*[c]

a) Corning European Technology Center, 77210 Avon, France.

b) Sorbonne Université, Muséum National d'Histoire Naturelle, UMR CNRS 7590, IRD, Institut de Minéralogie, de Physique des Matériaux et de Cosmochimie, IMPMC, 75005 Paris, France

c) Géomatériaux, CNRS-IPGP, Université de Paris, 75005 Paris, France.

*Corresponding author: neuville@ipgp.fr

ABSTRACT: Redox control of glasses is paramount to both their fusion process and to obtain the desired properties of high technological glasses. However, the link between melting parameters such as temperature, furnace atmosphere or quenching rate and the redox state of the final products is poorly understood. In this work, *in situ* XANES data at Ce L_3-edge data were acquired at high temperature on cerium containing sodium aluminosilicate glasses, allowing the determination of thermodynamic constants necessary to predict cerium redox state over a wide temperature range (900°C-1500°C). The results obtained were compared to Raman spectra of samples quenched from different temperatures. Our findings demonstrate that the quench performed was fast enough to block cerium oxidation state, meaning the redox measured at room temperature is representative of a high temperature state. This was further verified by room temperature Raman spectroscopy where a relationship was found between the spectra and melting conditions. Wet chemical analysis, XANES at Ce L_3-edge, Raman spectroscopy and optical absorption spectroscopy were successfully used to determine redox state of cerium in aluminosilicates.

1. Introduction

Cerium oxide is widely used in the glass industry, especially for advanced technological applications such as optical fiber where it reduces photodarkening[1–3], X-ray shielding[4,5], scintillator glasses for medical and nuclear safety applications[6–8], but also UV protection[9,10]. Cerium is a multivalent element, and is commonly found as a mixture of trivalent Ce(III) and tetravalent Ce(IV) ions in silicate glasses. The properties of cerium doped glasses are strongly dependent on the redox state of cerium. Indeed, the ability for cerium to limit photodarkening is due to Ce(III) being able to capture holes and photo-oxidize under UV, as well as Ce(IV) being able to capture an electron and get photoreduced under UV[2,3,11,12]. Cerium ions can then be brought back to their original state after a thermal treatment (thermal bleaching) or even at room temperature, thereby preventing the apparition of colored defects in the fiber. In a similar way, both Ce(III) and Ce(IV) species are important to obtain broad band UV shielding materials. Ce(IV) absorbs UV-B and UV-C due to a very intense Ce(IV)-O charge transfer absorption below 300 nm, whereas Ce(III) possesses an intense 5d→4f transition around 320 nm, covering UV-A[10]. For cerium doped scintillator glasses, only Ce(III) exhibits fluorescence and radioluminescence, making it the desired redox state for these applications[6,8]. However, studies suggest that Ce(IV) might have a positive impact by reducing the lifetime of Ce(III) luminescence, which is a key parameter for Positron Emission Tomography[8,13]. Therefore, controlling cerium redox is crucial to attain the desired properties of the finished materials.

Cerium oxide is also used as a fining agent in many industrial glass processes[14,15]. When added to the raw materials and melted, CeO_2 gets reduced and releases oxygen. This oxygen release helps already present bubbles to reach the critical size needed to escape the viscous melt. The release of oxygen bubbles greatly influences the melt properties, e.g. its rheology. Controlling this gas release is important to understand technological processes and previous studies have focused on this phenomenon[16]. The growth of oxygen bubbles during melting depends, among others, on the redox couple equilibrium of cerium at high temperature. Redox equilibria in melts are influenced by many parameters such as melting temperature, furnace atmosphere (oxygen fugacity), overall glass composition as well as the presence of other multivalent elements, even as impurities[17–21]. Understanding redox processes *in situ* could highlight complex reactions occurring in industrial furnaces, as well as enabling better control of cerium redox state to tune the properties of high technology glasses.

In this study, *in situ* XANES spectroscopy has been used to determine cerium redox equilibrium in the molten state as well as monitoring its evolution during quenching. The goal was to compare the *in situ* results with room temperature measurements performed with a variety of techniques. XANES, Raman spectroscopy, optical absorption spectroscopy and wet chemical analysis were all used to assess cerium redox state in aluminosilicate glasses.

2. Experimental Section

2.1 Glass synthesis. A total of 2 kg of cerium free sodium aluminosilicate glass was synthesized at Corning European Technology Center (Avon-France) at 1650°C from SiO_2, Na_2CO_3 and Al_2O_3. Sample homogeneity was checked using Raman spectroscopy. The obtained glass was then finely ground in an agate mortar with CeO_2 (99.9%, Alfa Aesar) to obtain doping between 400 ppm and 20000 ppm on a molar basis. The mixture was then melted 4 times, 2 hours each, at 1600°C in Pt crucibles to ensure homogeneity. For compositions with a CeO_2 concentration higher than 10 mol‰ (i.e. 10000 ppm), the temperature was slowly increased up to 1600°C to prevent overflowing because of bubble release. The liquids were then quenched by dipping the bottom of the Pt crucible into water. The obtained samples are named NASx with x the molar concentration of added CeO_2 in ‰ (per thousand) (e.g NAS0.4 is doped with 0.4 mol‰ or 400 ppm of CeO_2). Samples doped with CeO_2 concentrations higher than 5 mol‰ exhibit a slight yellow color. The glass compositions were measured by EPMA (see below) and reported in Table I.

Table I. Compositions (wt%) measured by EPMA as well as density and molar volume for the NASx glass series.

Sample	SiO_2	Al_2O_3	Na_2O	CeO_2	FeO[a]	Density (g.cm^{-3})	Molar Volume (cm^3.mol^{-1})[b]
NAS0	61.9 (8)	19.2 (3)	18.1 (3)	0	<0.005	**2.430 (1)**	**27.0 (3)**
NAS0.4	60.9 (9)	19.5 (2)	17.7 (3)	0.106 (4)	0.016 (2)	**2.431 (2)**	**27.1 (2)**
NAS2	61.6 (9)	19.7 (4)	17.1 (4)	0.50 (1)	0.038 (3)	**2.435 (2)**	**27.1 (3)**
NAS5	61.5 (9)	19.3 (4)	17.1 (4)	1.25 (2)	<0.005	**2.449 (2)**	**27.1 (3)**
NAS10	60.0 (8)	19.1 (4)	16.9 (4)	2.29 (2)	<0.005	**2.465 (4)**	**27.1 (3)**
NAS13	59.8 (9)	19.0 (4)	17.3 (2)	3.10 (1)	0.018 (5)	**2.481 (2)**	**27.0 (4)**
NAS20	59.3 (9)	18.6 (3)	16.4 (2)	5.02 (4)	<0.005	**2.521 (2)**	**26.9 (3)**

Note : Uncertainties on the last digit are given between brackets.
a) Total iron given as FeO. Iron should be treated as contamination.
b) Molar Volume is calculated from the measured density and the composition obtained by EPMA.

In order to investigate the influence of melting parameters on the room temperature redox state, melts were equilibrated at various temperatures as well as in reducing conditions.

Small amounts (less than 1 g) of NASx glass samples were equilibrated at different temperatures ranging from 1000°C to 1500°C for at least 6 hours in an electrical furnace. The obtained samples were then quenched by dipping the bottom of the Pt crucible in water. In order to obtain fully reduced samples, two distinct protocols were used. First, approximately 2 g of NAS10 were remelted at 1500°C in a graphite crucible (GC) for 2 hours. The obtained sample was poured on a copper plate and quenched by air. This sample is named NAS10_GC. For optical measurements, approximately 2 g of NAS0, NAS0.4 and NAS2 were remelted in alumina crucibles under an Ar 97.4%/H_2 2.6% atmosphere at 1350°C for 2 hours in a tubular furnace. The samples were allowed to cool down to room temperature within the furnace. These samples are denoted NAS0H2, NAS0.4H2 and NAS2H2, respectively. Sample homogeneity was checked using Raman spectroscopy, especially to ensure the absence of crystalline phases.

Glass density was measured using Archimedes' method using toluene as immersion liquid.

2.2 EPMA. Electron Probe Micro-analysis (EPMA) measurements were performed on a Cameca SX-Five at Camparis facility. A voltage of 25 kV and a beam size of 20 μm were used for all measurements. For Si, Na and Al, a current intensity of 4 nA was used, whereas a current intensity of 200 nA was applied to measure the low concentrations of Ce and Fe. The standards used were Albite (Na, Si), $(Mg,Fe)_3Al_2(SiO4)_3$ (Al), FeS_2 (Fe) and a reference glass for Ce. At least ten measurements were performed for each composition, with the average values reported in Table I.

2.3 Wet chemistry analysis. About 3 g of each sample were ground to a fine powder before being dissolved in a 3M HCl: 20M HF solution. After dissolution, concentrated boric acid was added to protect the titration flask from residual HF. The pH of the obtained solution was adjusted to 4 using an ammonium acetate buffer. Mohr salt ($Fe(NH_4)_2(SO_4)_2$) was then added to the solution to react with the Ce(IV) in solution. The remaining ferrous ions were then titrated using ferrozine with which they form a colored complex. The absorbance of the obtained solution at 562 nm was compared to a calibration curve established with a mono-elementary solution of $FeCl_3$ in ascorbic acid to ensure total reduction of the iron ions. The amount of Ce(IV) is determined by back titration from the difference between added Fe(II) and measured Fe(II). The experiment was conducted three times for each composition. The concentration of Ce(IV) was then divided by the total

amount of cerium measured by EPMA to obtain the redox ratio.

2.4 Optical Absorption spectroscopy. Optical absorption spectra were recorded using a Perkin-Elmer® Lambda 1050 UV-Visible-NIR spectrophotometer in transmission mode in the range 10000 cm^{-1}-55000 cm^{-1}. Double-sided mirror polished samples, with thickness ranging from 350 to 200 microns, were used. Given the small thickness of our samples, we were unable to measure samples with two different thicknesses to assess reflection, as performed by Vercamer *et al*.[22]. Instead, a simple linear background was fitted. Spectra are corrected by sample thickness but not normalized by total cerium concentration as both Ce(III) and Ce(IV) are present in our samples and each redox state possesses distinct absorption bands (see section 3.1 for details).

2.5 XANES. XANES spectra were recorded on two different beamlines at the SOLEIL synchrotron facility (Saint-Aubin, France) operating at 2.72 GeV and 500 mA.

Room temperature Ce L3-edge XANES spectra recorded on the LUCIA beamline were collected in fluorescence mode using a SDD detector[23]. A Si(111) double crystal monochromator was used for the incoming X-ray. The energy was calibrated at the first inflexion point of the Ti K-edge (4966 eV) using a Ti foil. A macro beam of 3x3 mm^2 was used to minimize photo-oxidation of the samples, at least three different scans, of five minutes each, were collected on all samples to evaluate possible photo-oxidation. Spectra were acquired in continuous mode (FLYSCAN) from 5680 eV to 5850 eV with a resolution of 0.2 eV and a duration of 300 ms per step.

Room temperature and *in situ* Ce L3-edge XANES spectra recorded on the ODE beamline were collected in dispersive transmission mode using a bent Si(111) monochromator[24]. Pixel to energy conversion was performed using polynomial fitting on a CeO_2 reference. Spectra were acquired from 5670 eV to 5855 eV with a 0.2 eV resolution using a beam size of 100*100μm^2, and collection times varied between 0.2 and 7 s. Room temperature spectra were collected on glass slices polished to the correct thickness. High temperature experiments were performed by loading glass powder in a 500 µm hole of 90Pt-10Ir wires. The wires were then heated by passing an electric current. Each wire was calibrated using the procedure detailed by Neuville and Mysen[25], see references therein for setup details. The obtained error on the temperature is conservatively set to ± 20°C. In order to limit volatilization effects, different samples were used for each temperature above 1400 °C. All XANES spectra were then processed using the Larch software[26]. Pre-edge and post-edge were fitted by linear functions for normalization. Fitting was performed by calculating linear combinations of end-members (see section 3.3 for details).

The use of two different beamlines was necessary as the ODE beamline is particularly well suited for *in situ* measurements. However, since the spectra were recorded in transmission mode, only samples with high cerium concentration could be effectively measured. The LUCIA beamline was used to measure cerium redox state at room temperature for all samples.

2.6 Raman spectroscopy. Vertical-Vertical (VV) and Vertical-Horizontal (VH) polarized, as well as unpolarized Raman spectra, were acquired using a Labram HR Evolution spectrometer equipped with a Peltier-cooled CCD and an 1800 lines per mm grating. The samples were excited with a Coherent MX 488 nm solid-state laser focused through a ×50 Olympus objective (LMplanFl, WD: 10.6 mm) on the sample surface. The spectral resolution of the setup is ~1.7 cm^{-1} and the spatial resolution is ~ 1 μm. The laser power at the exit was adjusted to 600 mW. Spectra were acquired from 20 cm^{-1} to 1500 cm^{-1} thanks to a ULF filter to attenuate the laser signal. A linear baseline was fitted over the 1350-1500 cm^{-1} range. Spectra fitting was performed using the Fityk software with the Levenberg-Marquardt method[27].

3. Results

3.1 Samples and physical property. Sample densities show a linear increase of 4% upon addition of CeO_2 from NAS0 to NAS20. This trend was previously observed in boro-aluminosilicate glasses[5] doped with up to 5 mol% CeO_2. Iron concentration is very low in the NAS0 glass (below the detection limit of 50 wt ppm of FeO). However some glasses show a higher amount of iron than expected, which can be due either to cross contamination by iron pollution of the crucibles or to the doping and remelting procedure. Although the concentration of iron is systematically inferior to the cerium one, its influence will be discussed in section 4.4.

3.2 Optical absorption spectroscopy. Only the UV region is of interest to determine cerium redox as the absorption of both Ce(III) and Ce(IV) occurs at higher wavenumbers than 25000cm^{-1}.

The spectra for the undoped-samples prepared in air and in reduced atmosphere, NAS0 and the NAS0H2 respectively, are different (Figure 1.A). This can be explained by the presence of iron as an impurity and a change in the redox state from Fe(III) in NAS0 to Fe(II) in NAS0H2. Since the transitions involved are Oxygen-Metal Charge Transfers (OMCT), these transitions are allowed and therefore very intense, explaining why they are visible even for low iron concentrations. The positions of their maximums are blueshifted by about 3500 cm^{-1} compared to the work of Vercamer *et al*.[22] possibly because our composition has a slightly higher optical basicity than the one they studied (0.57 vs 0.58 for NAS0), calculated according to Duffy[28]. An additional strong absorption band is visible above 48000 cm^{-1}, attributed to the absorption of the host alumino-silicate glass. Due to its intensity, all spectra saturate above 50000 cm^{-1}.

With CeO_2 addition, new features appear around 31000 cm^{-1} and 40000 cm^{-1} (NAS0.4, Figure 1.B, red curve). Upon reduction, the contribution at 31000 cm^{-1} does not change while the one around 40000 cm^{-1} diminishes sharply (NAS0.4H2, Figure 1.B, blue curve). Therefore, the absorption in the UV-B and early UV-C range (35710-50000 cm^{-1}) is due to Ce(IV), while the UV-A range (25000-31750 cm^{-1}) is covered by Ce(III)[10]. This highlights the importance of dual-valence in cerium doped UV-shielding glasses. The absence of variation of the absorption maximum at 31000 cm^{-1} upon cerium reduction (Figure 1.B) shows that the Ce(IV) contribution at this wavelength is not zero for the sample synthetized under air. Upon reduction the Ce(IV) absorption diminishes while the Ce(III) absorption increases. This leads to an overall stagnation of the absorption intensity at 31000 cm^{-1}, resembling an isosbestic point. This shows the importance of separating Ce(IV) and Ce(III) contributions before quantifying redox state.

Ce(IV) has the most intense contribution of the two redox states as its absorption is due to a very intense OMCT transition. Therefore, the linear absorptions in the UV region of samples equilibrated in air are high even for low cerium concentration (NAS0.4, Figure 1.B, red curve). To avoid saturation in the region of interest, it is necessary to prepare thin samples (thickness ≈170 μm for NAS2).

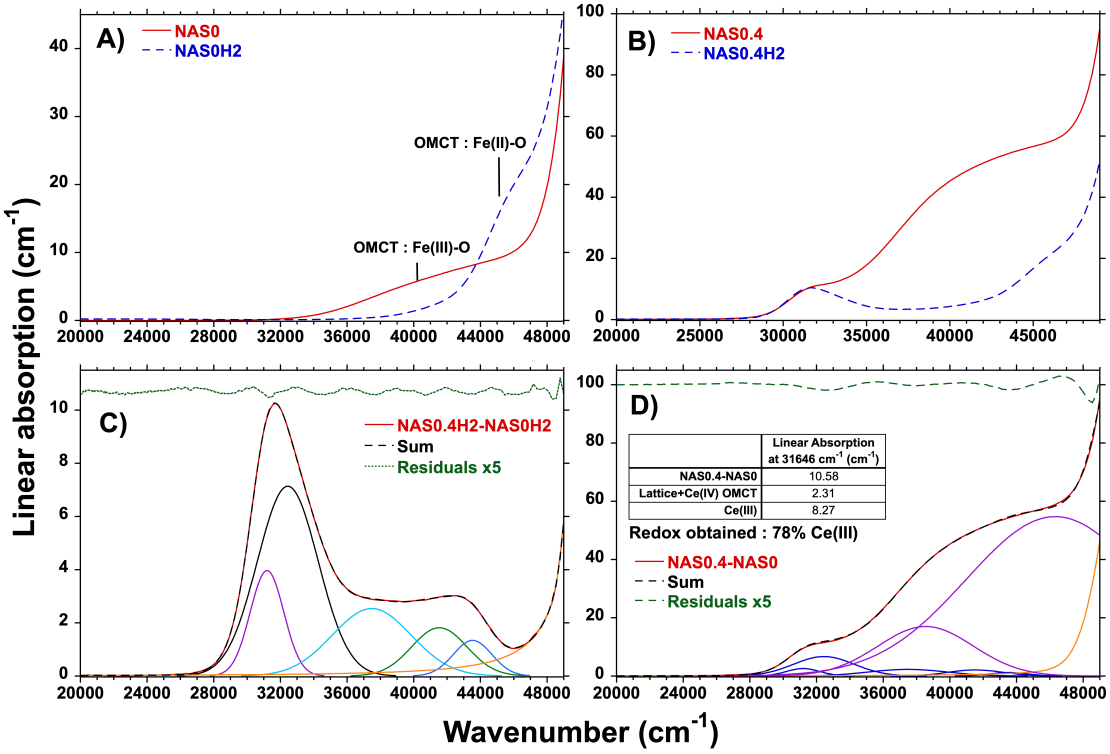

Figure 1. A) Optical absorption spectra of undoped NAS0 glass equilibrated in air (red curve) and in reducing atmosphere (blue curve), Fe-OMCTs contributions are highlighted B). Optical absorption spectra of NAS0.4 glass equilibrated in air (red curve) and in reducing atmosphere (blue curve). C) Decomposition of the optical absorption spectrum of NAS0.4H2 after subtracting the spectrum of the undoped NAS0H2 glass. Residuals (top dotted green curve) are multiplied by five for clarity, and the glass network absorption is also displayed (orange curve). D) Decomposition of the optical absorption spectrum of NAS0.4 after subtracting the undoped NAS0 glass spectrum, with Ce(III) absorption bands (blue), Ce(IV) absorption bands (purple) and glass absorption (orange). A linear background was subtracted to all samples to account for reflection.

To precisely determine the Ce contributions, it is necessary to subtract the contribution from the base glass synthesized under the corresponding atmosphere since we have shown that the absorption of the base glass is dependent on the synthesis conditions (Figure 1.A). The results of this subtraction are shown in figure 1.C and 1.D for sample NAS0.4H2 and NAS0.4 respectively. Given the high oxidation potential of the Ce(III)/Ce(IV) couple, it is assumed that Ce(III) is responsible for all of the absorption bands in samples melted under reducing conditions[29,30]. The electronic configuration of trivalent cerium is $[Xe]6s^0 5d^0 4f^1$ and the electronic transitions occur between the 4*f* and the 5*d* levels which, assuming no particular symmetry, are split in five sublevels[31]. Accordingly, five absorption bands have been used to decompose the broad UV band, as shown in Figure 1.C (note that a glass lattice absorption component above 48000 cm^{-1} is still needed, despite the subtraction of the contribution of the base glass). The five transitions used are not assigned to specific sublevels and their positions are not interpreted.

The absorption maximum of the Ce(III) contribution in the NAS0.4H2 spectrum was determined to be located at

31646 cm^{-1} (316 nm). Since Ce(III) is the only absorbing species at this wavelength, its molar absorption coefficient was found to be 713 ± 30 $L.mol^{-1}.cm^{-1}$, in good agreement with previously reported values[31,32]. Indeed, the transition is spin and symmetry allowed, making the *f-d* transitions more intense than *d-d* transitions for transition metals such as Fe.

In order to assess the redox state of the samples synthesized in air, it is necessary to determine the contributions for Ce(IV). First, the different contributions of Ce(III) were fixed (position and width) from the fit of the NAS0.4H2 spectrum (figure 1.C). The remaining absorption related to the glass network was modeled using a pseudo-Voigt function because of the small number of data points available for the fit (Figure 1.D, orange curve). The absorption attributed to Ce(IV) is due to OMCTs and is usually modeled in literature by using two Gaussian functions[31,32] (figure 1.D, purple curves). The intensity of the linear absorption for Ce(III) at 31646 cm^{-1} is 8.27 cm^{-1}, which gives a concentration of 310 ± 20 ppm for Ce(III) using the molar absorption coefficient previously obtained. Therefore, given the total Ce content in this glass, a redox state of 78 ± 5% Ce(III)/Ce_{tot} can be quantified.

Repeating the same procedure with the NAS2 samples (spectra for NAS2 and NAS2H2 are available in supplementary figure S.1) yields 64 ± 5 % Ce(III). Even considering that the contributions of Ce(IV) and lattice absorptions at 31646 cm^{-1} are zero, therefore overestimating the concentration of Ce(III), the obtained redox ratio would be of 71 ± 5 %, a value closer, but still less than the ratio obtained for the NAS0.4 sample. Consequently, the difference in redox ratio between different samples cannot be solely attributed to data processing. The spectrum for the NAS2H2 sample exhibits an abnormally strong absorption between 42000 cm^{-1} and 45000 cm^{-1}, in the Fe(II)-OMCT range. Considering the iron impurity levels reported in Table I, the iron concentration in sample NAS2 is much more important than the one in NAS0. Therefore, when subtracting the absorption of NAS0H2 from that of NAS2H2, the contribution of Fe-OMCTs do not cancel out. This impacts measurements of Ce(III) absorption in the reduced sample NAS2H2, which in turns affects the accuracy of cerium redox in NAS2.

3.3 XANES spectroscopy. Trivalent and tetravalent cerium display differences in the L_3-edge XANES region. As shown on figure 2.A, Ce(III)PO_4 possesses a narrow white line with a maximum around 5727 eV. On the same figure, Ce(IV)O_2 exhibits two absorption peaks at higher energies, 5731.5 and 5738 eV respectively. This difference allows us to determine, by linear combination, the redox ratio of cerium in our samples.

The XANES spectrum of the reduced NAS10_GC sample is very close to the Ce(III)PO_4 (monazite) reference (see Figure 2.A.). The difference can be attributed to differences in the local site geometry and coordination of Ce. Indeed the first EXAFS oscillation is shifted from 5759 eV in Ce(III)PO_4 to 5761 eV in NAS10_GC. This qualitatively indicates shorter Ce-O bond lengths and therefore a smaller Ce coordination number in NAS10_GC than in $CePO_4$. This is consistent with the work of Rygel *et al.*[33] who found a coordination number around 7 for Ce(III) in aluminophosphate and silicophosphate glasses, whereas Ce is 9-fold coordinated in $CePO_4$[34].

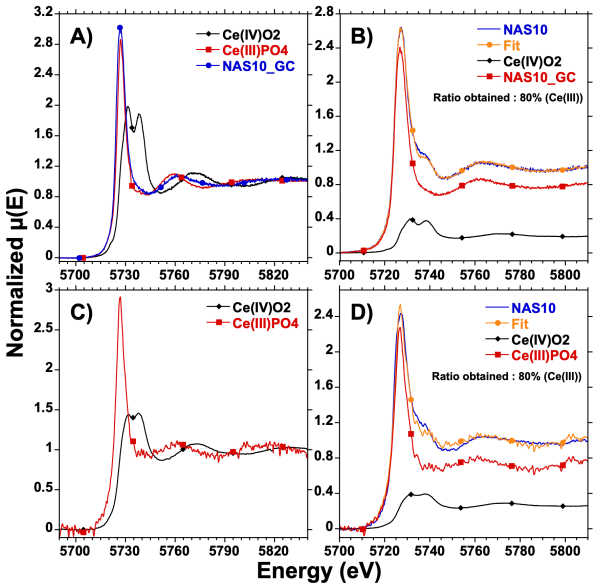

Figure 2. A) Ce L3-edge flattened XANES spectra of references obtained in fluorescence mode on the LUCIA beamline. B) Example of linear combination performed on the LUCIA data. C) Ce L3-edge flattened XANES spectra of references obtained in transmission mode on the ODE beamline. D) Example of linear combination performed on the ODE data.

NAS10_GC is used as the Ce(III) end-member for the linear combinations of the LUCIA data, whereas Ce(III)PO_4 serves for the linear combinations of the ODE data since the NAS10_GC spectrum was not acquired on this beamline. The discrepancy in measured redox state on the LUCIA beamline using Ce(III)PO_4 or NAS10_GC as the Ce(III) end-member is minor. For instance, in the case of NAS10, as illustrated in Figure 2, using Ce(III)PO_4 yields a redox state of 82±3 % (Ce(III)) while using NAS10_GC yields a redox state of 80±3 % (Ce(III)), the fit quality is comparatively lower. Crystalline Ce(IV)O_2 is selected as the Ce(IV) end-member since fully oxidized cerium is difficult to obtain in silicate glass due to the low solubility of Ce(IV) as well as the high redox potential of the Ce(III)/Ce(IV) couple[29,35,36].

As shown in Figures 2.B and 2.D, this difference in end members and in collection mode has no significant influence on the results. The cerium redox state determined from fitting with a linear combination is 80% Ce(III), in agreement with previous studies performed on glasses with similar optical basicity[29,36–38]. The fits displayed in Figures 2.B and 2.D show a deviation in the data around 5735 eV which is attributed to the choice of crystalline Ce(IV)O_2 as the Ce(IV) end member. Indeed, using a crystalline end

member to fit XANES of glassy sample often yields deviations due to a difference in the probed local environment of the element. Crystalline Ce(IV)O_2 was chosen as the Ce(IV) reference to guarantee that the end-member is fully oxidized rather than using a partially oxidized glass that would have likely entailed a systematic error in the linear combination analysis.

As X-ray irradiation can affect the measured redox state of samples at room temperature, we verified that no photo-oxidation phenomena occurred during the time span of the measurements. No photo-oxidation was observed on the LUCIA beamline except for the NAS0.4 sample whereas photo-oxidation was observed on the ODE beamline even for the NAS20 sample. However, the photo-oxidation kinetics are slow enough not to affect the measurements performed (see supplementary figure S.2 for details).

3.4 Raman spectra. When CeO_2 is added to the glass, the main change in the Raman spectra occurs within the 800-1100 cm^{-1} range (Figure 3). A contribution at ≈ 975 cm^{-1} is clearly increasing in intensity with the addition of CeO_2, and this contribution is more visible when examining the VH spectra. Additionally, an overall blueshift of the 800-1250 cm^{-1} band is observed with cerium addition. This is due to the addition of a heavy ion in the glass, changing the overall oscillator strengths of the glass.

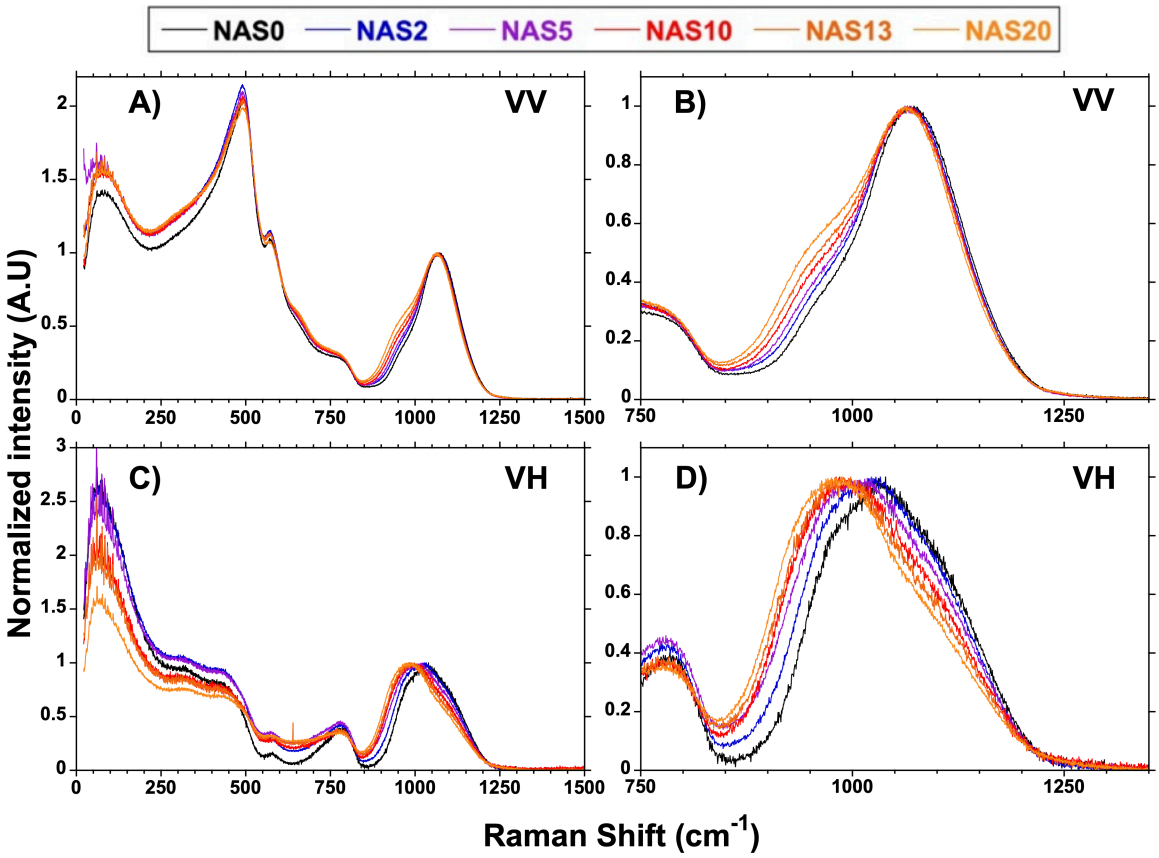

Figure 3. A) VV and B) VH polarized Raman spectra of NAS doped with CeO_2. B) and D) are the region of interest of A and C respectively. All spectra are normalized so that the maximum intensity in the 800-1350 cm^{-1} range is equal to 1.

To fit both the VV and the VH spectra without changing their relative intensity, a simple constant background was applied to the 1350-1500 cm^{-1} region (Figure 4). Two Gaussian functions were used to fit the background in the low wavenumber region, with the position of background (II) being set to 873.15 cm^{-1}. The fitting parameters of those gaussians are not interpreted. The depolarization ratio $\rho = Intensity(VH)/Intensity(VV)$ was calculated using raw data as the VV and VH spectra were performed on the exact same spot on the sample with the same acquisition parameters. The HWHM and position of each band are identical between the VV and VH polarized decompositions. Table II shows the evolution of the decomposition parameters when CeO_2 is added to the glass. An example of decomposition is shown in Figure 4 for NAS0 and NAS10 samples and additional decompositions are available in Figure S.4.

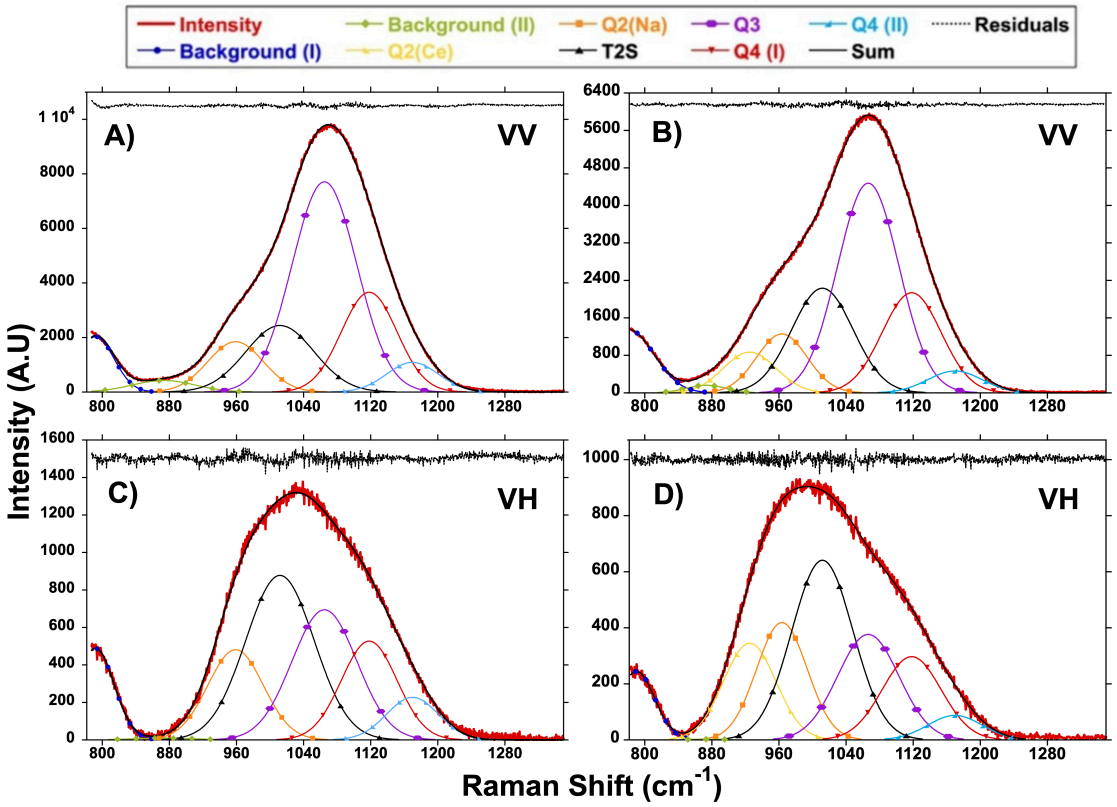

Figure 4. Decomposition of the VV and VH polarized Raman spectra for the NAS0 sample, A) and C) respectively. Decomposition of the VV and VH polarized Raman spectra for the NAS10 sample, B) and D) respectively.

Table II. Raman decomposition parameters for the NASx series.

Band		NAS0	NAS2	NAS5	NAS10	NAS13	NAS20
Q^2(Ce)	Position (cm^{-1})		925.1	925.1	925.1	925.1	925.1
	Relative area (%)[a]		2.4±0.8	5.1±0.6	6.8±.6	7.8±0.6	10.5±0.8
	Depolarization ratio (ρ)		0.32	0.35	0.39	0.38	0.60
Q^2(Na)	Position (cm^{-1})	958.9	958.9	960.9	963.5	963.5	966.5
	Relative area (%)	10±0.8	10±0.8	9.2±0.8	10±0.8	10±0.8	10.7±0.8
	Depolarization ratio (ρ)	0.27	0.33	0.34	0.34	0.31	0.49
T_{2S}	Position (cm^{-1})	1011.8	1011.8	1011.8	1011.8	1011.8	1011.8
	Relative area (%)	16±1	19±1	20±1	20±1	21±1	21±1
	Depolarization ratio (ρ)	0.33	0.3	0.31	0.29	0.28	0.45
Q^3	Position (cm^{-1})	1064.8	1064.8	1064.8	1066.4	1066.4	1066.4
	Relative area (%)	49±2	44±2	42±2	41±2	40±2	39±2
	Depolarization ratio (ρ)	0.09	0.10	0.09	0.08	0.07	0.12
Q^4(I)	Position (cm^{-1})	1118.1	1118.1	1118.1	1118.1	1118.1	1118.1
	Relative area (%)	20±1	21±1	21±1	19±1	18±1	16±1
	Depolarization ratio (ρ)	0.14	0.15	0.15	0.14	0.14	0.22
Q^4(II)	Position (cm^{-1})	1169.8	1169.8	1169.8	1169.8	1169.8	1169.8
	Relative area (%)	5.5±0.6	4.4±0.6	3.8±0.8	3.8±0.8	3.6±0.8	3.3±0.8
	Depolarization ratio (ρ)	0.21	0.21	0.18	0.19	0.16	0.28

Note: Complete decomposition parameters, including HWHM and peak intensities are given in supplementary Table I.
a) Relative area given for the VV polarized spectra

The decomposition of the base NAS0 glass was done following a previous investigation[39]. Considering Figure 4.A, five bands were used to explain the 800-1300 cm^{-1} region which is associated to vibrations of the TO_4 tetrahedra (with T=Si, Al)[40].

In agreement with previous studies, the band centered around 959 cm^{-1} was attributed to A_1 vibrations of Q^2 units, the band centered around 1065 cm^{-1} was attributed to A_1 vibrations of Q^3 units[39,41,42]. The vibrations centered around 1120 cm^{-1} and 1170 cm^{-1} are attributed to A_1 vibrations of Q^4 units. The presence of two distinct bands, labelled Q^4(I) and Q^4(II), is necessary to explain the high wavenumber domain of this region. However, this does not indicate two distinct Q^4 environments but rather an asymmetry in one environment and especially in the T-O-T bond angle, as attributed by Seifert *et al*.[43]

The band centered around 1010 cm^{-1} was attributed to a T_2 asymmetric stretching vibration of the SiO_4 tetrahedron[40,44,45], labelled T_{2s}. This vibration concerns all Q^n units and therefore it covers a much broader range of vibrations than the other A_1 stretching vibrations. This could explain why the T_{2s} band appears to be the broadest one in our decomposition (around 48 cm^{-1} HWHM).

The symmetry of vibrations is particularly important when comparing VV and VH polarized spectra. Indeed, symmetric vibrations such as the A_1 bands are expected to be completely polarized ($\rho = 0$)[46,47]. However, because our system is amorphous, SiO_4 tetrahedra do not have perfect T_d symmetry, which therefore slightly depolarizes A_1 vibrations. This phenomenon has been evidenced in multiple amorphous systems, including silica glass, and explains why the depolarization ratios reported in Table II are not zero for the Q^n species[40,48–50]. The depolarization ratio of the T_{2s} band is 0.33 for NAS0 glass, consistent with an asymmetric stretching band. This explains why the relative intensity of the T_{2s} band is more important in the VH polarized spectra (Figure 4.C) than in the VV polarized spectra (Figure 4.A).

In addition to the bands of the undoped NAS0 glass discussed above, addition of CeO_2 leads to the apparition of a new Raman band (Figure 4), labelled as Q^2(Ce) in the decomposition, whose assignment will be discussed in section 4.5.

4. Discussion

4.1 Technique comparison. Cerium redox state was assessed using three different techniques: XANES spectroscopy, wet chemical analysis, and optical absorption spectroscopy. Redox ratios obtained for the NASx series are shown in Table III.

Table III. Cerium redox measured at room temperature by different techniques for samples of the NASx series.

	%Ce(III)			
Sample	**XANES (LUCIA)**	**XANES (ODE)**	**Wet chemistry**	**Optical spectroscopy**
NAS0.4	93±3		84±2	78±5
NAS2	79±3		82±2	64±5
NAS5	79±3		83±2	
NAS10	80±3	80±3	79±2	
NAS13	79±3	78±3	82±2	
NAS20		81±3		

As shown in Figure 2, XANES measurements performed on ODE and LUCIA beamlines yield similar results, and their redox values are comparable within uncertainties to those obtained by wet chemistry, indicating that cerium redox is maintained during the dissolution used in the latter. Cerium redox state also appears to be independent of concentration in the 2‰ to 20‰ range and close to 80% Ce(III); to our knowledge, this has not been reported before. Cerium in the NAS0.4 glass appears more reduced in XANES and optical spectroscopy than the other glasses, this will be further discussed in section 4.6.

Indeed, both the absorption bands of Ce(III) and Ce(IV) are very intense, increasingly thinner polished samples (around 150 μm for NAS2) are required as CeO_2 doping increases. The small thicknesses restrict the use of optical absorption spectroscopy to the investigation of cerium redox state in samples with low cerium concentration. Unfortunately, as shown by EPMA measurements, both NAS0.4 and NAS2 are contaminated by iron. This is an issue for the redox determination of cerium as iron possesses very strong absorption in the same spectral region (see section 3.2 for details). Therefore, optical

absorption spectroscopy seems promising for measuring cerium redox state of low doped samples with small iron contamination. This is the case of optical fibers made using the Modified Chemical Vapor Deposition process (MCVD). As they are not contaminated by iron and sometimes incorporate cerium in order to reduce photodarkening[1,3].

4.2. Cerium redox in the molten state. In order to determine the temperature dependence of cerium redox, samples were equilibrated in the 90Pt-10Ir wire microfurnace until no variation of the XANES spectra was observed. Considering the small sample volume involved in the measurement, equilibration times were relatively short, ranging from 5 minutes at 1500 °C to 2 hours at 900 °C. These values are consistent with previous studies involving iron[20,51,52]. As expected, an increase in temperature leads to a reduction of cerium (Figure 5 A and B), from 42% Ce(III) at 900 °C to 77% Ce(III) at 1500 °C. No measurements were performed between 1100 °C and 1300 °C as CeO_2 crystallized in bulk for these temperatures. For the measurements at 1000 °C and 1100 °C, mild CeO_2 surface crystallization was observed (see Supplementary Figure S.3 for an example). However, since the measurements were performed in transmission mode, the bulk of the glass was probed, mitigating the influence of surface phenomena such as surface crystallization on the measured redox state. Moreover, no slow oxidation was observed during the continuous monitoring of the XANES spectra once the redox equilibrium was reached at a given temperature. Therefore, the impact of crystallization on the overall redox state was considered negligible.

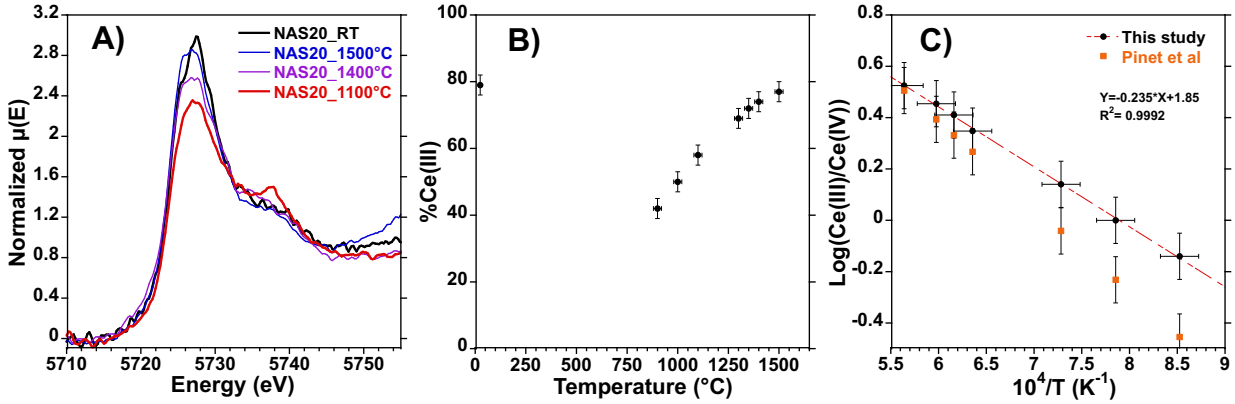

Figure 5. A) Normalized Ce L3-edge *in situ* XANES spectra of the NAS20 sample equilibrated at different temperatures. B) Evolution of cerium redox state as a function of temperature measured by *in situ* XANES spectroscopy. The point at room temperature is obtained for a glass quenched from 1600 °C. C) Comparison between the data obtained and the model of *Pinet et al*.[18]

As shown in Figure 5.C, the relationship between log(Ce(III)/Ce(IV)) and the reciprocal temperature is linear over the range of temperature studied. We consider the following chemical reaction for the redox equilibrium:

$$Ce^{4+}_{melt} + O^{2-}_{melt} \leftrightarrow Ce^{3+}_{melt} + \frac{1}{2}O_{2(g)}. \quad (1)$$

Equations (2) and (3) below highlight the relationship between the redox ratio and thermodynamic constants, notably the reduction enthalpy, $\Delta_r H$, as well as the reduction entropy, $\Delta_r S$:

$$2.303RT * \log([Ce(III)]/[Ce(IV)]) + 2.303RT/4 * \log(fO_{2(g)}) = -\Delta_r H - T\Delta_r S. \quad (2)$$

$$\log([Ce(III)]/[Ce(IV)]) = -\Delta_r H/2{,}303RT - C. \quad (3)$$

With R, the universal gas constant (8.314 J.K^{-1}.mol^{-1}), T, the temperature in Kelvin, fO_2, the oxygen fugacity and C, and constant with respect to temperature.

However, equation (1) only relates to the formal charge on cerium, without taking into account the coordination of cerium ions. Therefore, potential changes in coordination number during reduction are not considered and the actual reaction may be more complicated than the simple relation in equation (1)[53,54].

With the approximation that $\Delta_r H$ and $\Delta_r S$ are both independent of temperature over the range studied, Eq.3 becomes a linear relationship between $\log([Ce(III)]/[Ce(IV)])$ and the reciprocal temperature. This approximation was done in several previous studies on redox in silicate melts[35,55,56] and a linear relationship fits our data well (see Figure 5.C), with the following parameters obtained:

$\Delta_r H = 45.0 \pm 0.8$ kJ.mol^{-1} and

$\Delta_r S = 39 \pm 0.8$ J.mol^{-1}.K^{-1}

Moreover, deriving equation 2 from equation 1 assumes that the activity coefficients of Ce(III) and of Ce(IV) are similar, but also that the activity of O^{2-}_{melt} is equal to 1[18]. These assumptions only affect the calculation of $\Delta_r S$, whose value is given assuming an oxygen fugacity of 0.21. Such values are well in line with those obtained for similar systems[16,55], including the model by Pinet *et al.*[18] for temperatures higher than 1573 K, despite their model being based on lower temperature measurements (1178 K to 1516 K). However, cerium is found to be more reduced than predicted for temperatures lower than 1100 °C. This deviation can be explained by the difference in compositions since the Pinet model was built using borosilicate and alkali-silicate glasses rather than aluminosilicate glasses.

4.3. Evolution of cerium redox state during quenching. The redox state measured at room temperature does not follow the trend observed at high temperature, as is clearly visible in figure 5.B. Using the thermodynamical constants determined above, the expected equilibrium redox state at room temperature is 0% Ce(III) compared to the 81% Ce(III) measured. This implies that the redox ratios measured using both XANES and wet chemistry are out of equilibrium.

The evolution of cerium redox state was measured after cooling from 1500 °C to 620 °C (Tg = 612 °C, obtained through DTA with a 10°C.min^{-1} ramp). Due to the small scale of our sample in the micro-heating device, the time required to reach the desired temperature is short and conservatively estimated at 10 seconds, therefore, the first measurement is performed after reaching the target temperature. As shown in Figure 6, the cerium redox state does not vary significantly from 1500 °C to 620 °C, this observation holds particularly considering that, using the thermodynamical constants determined in section 4.3, the expected redox state at 620°C is 14% Ce(III).

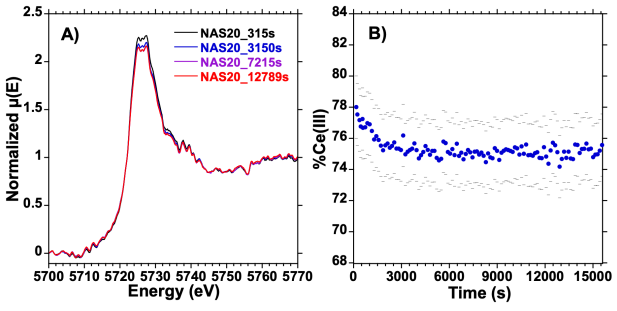

Figure 6. A) Flattened Ce L_3-edge *in situ* XANES spectra of the NAS20 sample at different times after a temperature decrease from 1500°C to 620°C. B) Evolution of cerium redox state after a temperature decrease from 1500°C to 620°C. Each data point corresponds to an average of 10 spectra. Only the caps of the error bars are drawn for clarity. The temperature change was achieved in less than 10 s, before the acquisition of the first spectrum.

The change in redox state during the first 3000 s does not appear to be significant, especially considering that the decrease in the Ce(III) contribution to the edge is not accompanied by an increase in the Ce(IV) contribution (Figure 6.A). We can therefore conclude that cerium redox state at room temperature is out of equilibrium and only representative of the redox at high temperature (here 1600 °C) if the quench is fast enough.

Considering that cerium is the only multivalent element present in the glass at concentrations of 2‰ and higher, the mechanism governing its reoxidation during cooling is diffusion controlled. Indeed, for cerium to oxidize, it has to give an electron to another species. The electron transfer in itself is very fast and, thereby, the limiting reaction is the diffusion of the other species to cerium. It is therefore interesting to compare the time scales on which the quench and the diffusion driven equilibration would occur in our system. Diffusion driven redox equilibration in glasses is governed by the diffusion of oxygen at high temperature, and the diffusion of network modifiers at low temperatures[20,52,57]. Since these diffusion coefficients are independent of the nature of the multivalent element studied, redox diffusion coefficients measured on iron containing melts can be applied to our system. The models presented in Figure 7 are based on the values obtained by Magnien *et al.*[52] for iron equilibration diffusion coefficients in pyroxene glasses. The glass composition of the present study is more viscous than the one used for the model, therefore, the rate of the equilibration processes is overestimated in Figure 7.

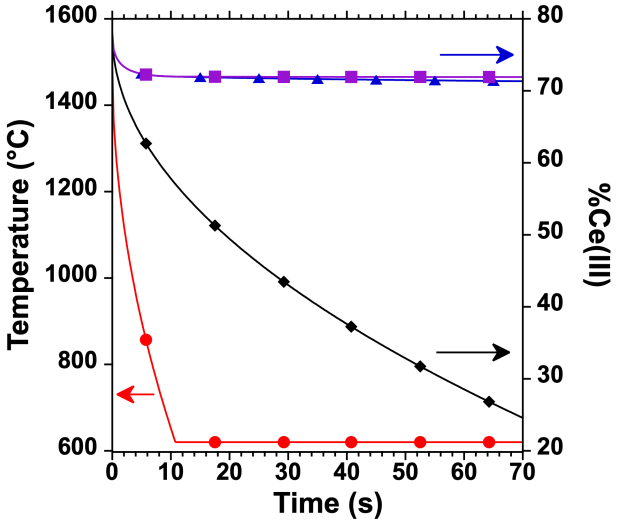

Figure 7. Modeled evolution of sample temperature during the cooling from 1500°C to 620°C (red circles). Modeled evolution of cerium redox state using a constant diffusion coefficient D=1.1x10^{-10} m^2.s^{-1} (black diamonds), a diffusion coefficient with an Arrhenius behavior as a function of temperature (blue triangles) or a diffusion coefficient with an Arrhenius behavior at high temperature with a different value near Tg (D=1x10^{-15} m^2.s^{-1}) (Purple squares). See text for details.

Diffusion controlled processes exhibit a linear relationship with the square root of time[58], with the

following equation relating time, t, diffusion coefficient, D, and the depth affected by equilibration, d:

$$d = \sqrt{4 * D * t} \quad (4)$$

The redox state of the sample is the weighted average between the redox state of the glass that has reequilibrated, over the thickness d, and the glass that has yet to be reequilibrated, over the thickness L-d, with L the total thickness of the sample. Here, L is estimated to be 300 μm, corresponding to the thickness of the sample in the 90Pt-10Ir wire.

Since the redox state at 1500 °C was determined by *in situ* XANES to be 78% Ce(III) and the equilibrium at 620 °C is expected to be 14% Ce(III) according to the constants determined in section 4.2, the general equation used for the model is:

$$\frac{[Ce(III)]}{[Ce(tot)]} = \frac{0.78*(L-d)+0.14*d}{L} \quad (5)$$

The first model considers the redox diffusion coefficient to be constant with a value of 1.1×10^{-10} $m^2.s^{-1}$. This value is the one determined by Magnien *et al*[52] for a temperature of 1500 °C. This underestimates greatly the equilibration time, making it comparable to the time scale of the temperature change, as the equilibrium redox state of 14% Ce(III) is attained after 100 seconds, see Figure 7.

The second model uses a diffusion coefficient with an Arrhenius dependence with temperature, as diffusion is thermally activated (see Magnien *et al*.[52] for the values used). In this scenario, the cerium redox state changes from 78% Ce(III) to 73% Ce(III) during the temperature change. Moreover, the redox state after 15000 s is still 65% Ce(III). The equilibrium redox state is reached only after 236 hours.

However, an assumption of the second model is that the diffusion processes involved in the molten state and near Tg are the same. This assumption is likely not valid on a wide temperature range as the nature of the diffusive species changes with temperature[20,52,57]. Indeed, the diffusion in the molten state is driven by oxygen diffusion whereas network modifiers are involved at lower temperatures.

Therefore, a third model uses a value for the diffusion coefficient at 620 °C of 1.10^{-15} $m^2.s^{-1}$ (given by Magnien *et al*. at Tg[52]) that is different from the value of $8.8.10^{-14}$ $m^2.s^{-1}$ that can be extrapolated from the Arrhenius relationship[52]. In this case, the cerium redox state still changes from 78% Ce(III) to 73% Ce(III) during the temperature change. However, the redox state after 15000 s is 71% Ce(III), and the equilibrium is reached after about 870 days, meaning that, once the temperature change has occurred, diffusion processes operate on a different time scale than the experiment performed in Figure 6.B. This would be even more pronounced in a crucible or in a furnace, where diffusion processes will be even slower considering the much larger volume of glass.

Considering the third model described previously, it is clear that diffusion is unable to compete with the quenching rate of the glass, confirming the results of figure 6.B, where the redox ratio observed near Tg is representative of a high temperature state.

4.4. Influence of iron impurities. As shown by EPMA in Table I, some of our samples are contaminated by iron. In the case of NAS0.4, the concentration of FeO (≈160 wt ppm or 140 mol ppm) cannot be neglected compared to the 410 mol ppm of CeO_2. Indeed, iron and cerium are known to interact with each other, as tetravalent cerium is used to oxidized ferrous ions to ferric ions[29,30].

This mutual interaction explains why the cerium redox state found for the NAS0.4 sample is more reduced than for the rest of the NASx series in XANES and optical absorption spectroscopy. As discussed previously, the cerium redox state at room temperature is representative of a high temperature equilibrium and, similarly, it is suitable to consider iron redox in the molten state (i.e at 1600 °C since it is the used melting temperature). Using Kress and Carmichael's model of iron redox state in melts[59], the expected redox state of iron in the NAS0 lattice at 1600°C is approximately 25% Fe(II). This would lead to a concentration of Fe(II) of 40 mol ppm in the glass at 1600 °C. On the other hand, according to XANES results, the measured redox state of cerium in the NAS0.4 sample is 93% Ce(III) compared to the 80% Ce(III) observed at higher concentrations. This corresponds to a decrease of 53 mol ppm of Ce(IV) in the glass, comparable to the amount of ferrous iron expected in the glass. The same difference is observed in optical absorption spectroscopy even though the values found for cerium redox state are different (see Table III).

The redox state of the iron impurities in both NAS0.4 and NAS2 was determined by wet chemistry as part of the standard protocol for measuring cerium redox state (see experimental section for details). In both cases, iron was determined to be fully oxidized at room temperature. Considering the diffusion models shown in Figure 7, it seems unlikely that iron was able to reequilibrate during quench. Another plausible explanation is that iron reacted with cerium through the following reaction:

$$Ce(IV) + Fe(II) \rightarrow Ce(III) + Fe(III) \quad (6)$$

Unfortunately, the results presented here do not allow us to conclude if this reaction occurs in the molten state or during quenching through a charge transfer process[60]. Regardless, this confirms that multivalent elements interact with one another, even at impurity levels. Schreiber *et al*.[30] reports the existence of a Ce(III)-O-Fe(III) linkage in silicate melts through EPR. The presence of this bond further points toward there being an interaction between these elements.

4.5. Cerium local environment. Upon addition of CeO_2 in the glass, the addition of a new Raman band is necessary to fit these data, especially for the VH polarized spectra (see Fig. 4). The position of the new band is centered around 925 cm^{-1} and remains constant with the amount of cerium added. We attribute this band to the formation of Q^2 species where at least one of the two non-bridging oxygens (NBO) is interacting with a cerium ion. This band is denoted Q^2(Ce) to differentiate it from the Q^2(Na) species already present in the cerium-free glass. Other studies have shown the rise of such a contribution upon addition of lanthanide ions in silicate glasses[61–63]. These studies report the presence of Q^2 and/or Q^3 species at least partly compensated by rare earth ions. The existence of a Si-O-Ce bond in a borosilicate glass was also evidenced by surface techniques such as XPS[64]. In the present study, only a Q^2(Ce) band could be justified in the decomposition. However, looking at Table II as well as Figure 8, both an increase of the relative area of the T_{2s} band and a decrease in depolarization ratio can be noted upon addition of CeO_2, this might indicate the presence of a weak Q^3(Ce) band. Since a Q^3 vibration possesses A_1 symmetry, its depolarization ratio is lower than that of the T_{2s}. However, without any supporting evidence for the existence of such a species in these glasses, its possible presence will not be discussed further. The difference in position between Q^2(Ce) and Q^2(Na) units is of about 35 cm^{-1} and is possibly due to the higher field strength of Ce^{4+} and Ce^{3+} relative to Na^+. Indeed, an increase in ionic field strength of the modifying cation leads to a polarization of the Si-NBO bond, decreasing the force constant of the corresponding vibration and shifting it to a lower wavenumber in the Raman spectra[63].

The apparition of a Ce-NBO related vibration in the Raman spectra upon cerium addition can be linked to previous studies performed on rare-earth doped silica fiber. Indeed, it has been shown that the introduction of non-bridging oxygen in those systems is necessary to ensure solubility and prevent clustering[65,66]. This behavior was attributed to rare-earth ions, including cerium, requiring non-bridging oxygens to ensure their high coordinence[67]. This further points to a Ce-NBO proximity in the glass network.

The dependence on CeO_2 content of the decomposed Raman bands suggests that cerium acts as a network modifying cation, diminishing glass polymerization, as the appearance of the Q^2(Ce) band appears to occur mainly at the expense of the Q^3 band, with very little change in any of the other peaks (Figure 8). Both Q^4 peaks may also decrease slightly in relative area with CeO_2, suggesting that cerium addition leads to network depolymerization, even though the changes in Q^4 band intensities are much smaller than that of the Q^3 band. A similar network depolymerization effect was observed in glasses doped with other rare earth cations[62,63,68–70].

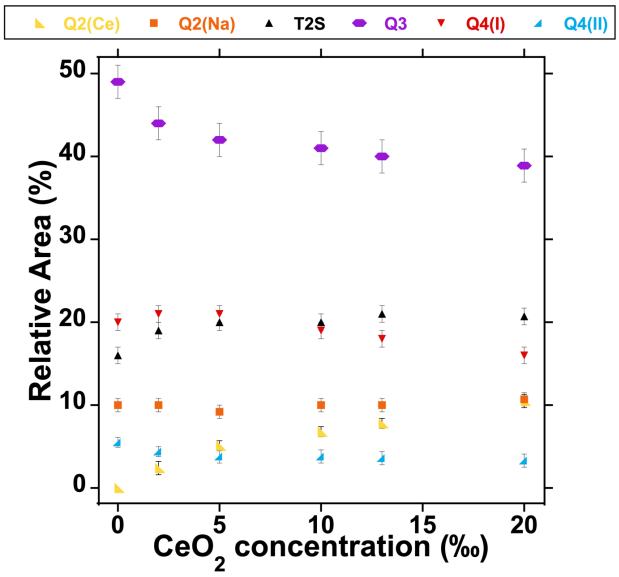

Figure 8. Evolution of the relative area of the different Raman bands presented in Figure 4 as a function of CeO_2 concentration. Full details are provided in Table II. Decompositions are available in Figure 4 and Figure S.4.

Of note, the depolarization ratios, ρ, found for the NAS20 sample are much higher than for the other samples (see Table II). This is particularly evident for the Q^2(Ce) vibration for which ρ reaches 0.6, an unusually high value for a vibration with A_1 symmetry. However, because the excitation wavelength is 488 nm and the samples become increasingly yellow upon addition of cerium, it is possible to observe resonant Raman phenomena (see Figure S.5 for absorption spectra of NAS20). These phenomena occur when the excitation wavelength used is within an absorption band of the sample and can greatly influence the polarization ratio of the observed transition[71,72]. Resonant Raman tends to exalt vibrations linked to the absorbing atom. In this case, the absorption involved is the Ce(IV)-O OMCT. This can explain both why the depolarization ratios greatly increase from NAS10 to the NAS20 sample, but also why this increase is more pronounced for the Q^2(Ce) band. Performing the measurements using lasers with higher wavelengths, such as 532 nm, should prevent this effect from occurring.

It is important to note that, according to section 4.2, both Ce(IV) and Ce(III) are present in the glass. In order to assess the role of each valence state on the Raman spectra, samples were equilibrated at different temperatures before being quenched. As shown in section 4.3, the redox state at room temperature is representative of the equilibrium state in which the system was at the time of quenching.

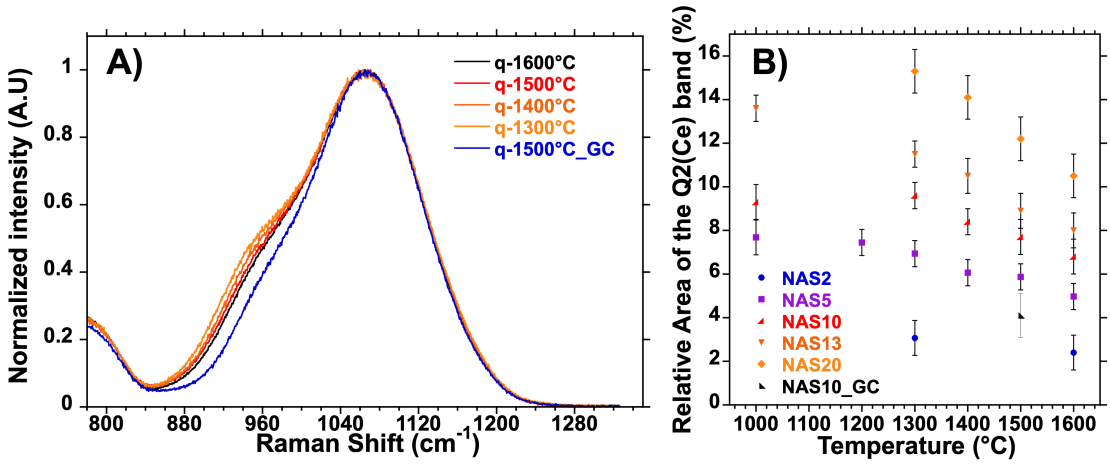

Figure 9. A) NAS10 samples equilibrated and quenched from different temperature. 1500°C_GC corresponds to the NAS10_GC sample, which was equilibrated in a graphite crucible at 1500 °C. All spectra are normalized so that the maximum intensity is equal to 1. B) Relative area of the Q^2(Ce) band of NAS glasses doped with different amount of CeO_2 as a function of equilibration temperature before quenching.

The glasses equilibrated at 1000°C do not follow the same trend as the ones equilibrated at higher temperatures. This discrepancy arises due to mild surface crystallization of CeO_2, as observed in Figure S.3. Since CeO_2 crystallizes, the concentration of cerium in the residual glass is reduced, explaining why the relative area of the Q^2(Ce) band is lower than expected. For the same reason, no melts were equilibrated at 1100°C or 1200°C since the crystallization of CeO_2 occurs in the bulk of the glass at these temperatures.

As shown on figure 9, when the equilibration temperature increases (*i.e* when the melt is reduced), the relative area of the Q^2(Ce) band decreases. This dependence strongly suggests that Ce(IV) contributes to this vibration. However, the Q^2(Ce) vibration is still detectable for the NAS10_GC sample, which was determined to be fully reduced using XANES spectroscopy. This observation indicates that both valence states contribute to this vibration, contrary to the vibration due to tetrahedral ferric ions that is specific to one oxidation state and environment of iron[51,73].

Given that a change from 80% Ce(III) to 100% Ce(III) is responsible for a doubling of the relative intensity of the Q^2(Ce) band, tetravalent cerium seems to be the main contributor. This points toward trivalent and tetravalent cerium occupying different local environments as well as Ce(IV) having a stronger depolymerization effect on the glass network A plausible interpretation is that trivalent cerium preferentially forms bonds with Q^3 units in the glass. Upon oxidation, the additional positive charge on tetravalent cerium requires the presence of another negative charge, typically in the form of a NBO, thus favoring the formation of Q^2(Ce) units.

Ce(III) and Ce(IV) having different local environments in glasses was evidenced by optical absorption measurements performed on photoionized cerium containing silicate glasses, showing that photo-oxidized Ce^{3+} and Ce^{4+} ions do not have the same absorption spectra[12]. Indeed, photoionized Ce^{3+} ions change valence state without changing environment and these ions are named Ce^{3++} in literature, to emphasize that they are tetravalent cerium ions with a trivalent cerium environment.

These observations show that the oxidation of Ce(III) to Ce(IV) is most likely accompanied by a change in local structure, possibly in terms of coordination number. These changes require the breaking and formation of chemical bonds, such structural rearrangements are slower reactions than electron transfers and are therefore very sensitive to quenching rate. This can explain why a partial reequilibration of cerium redox state is not observed during the quenching process (Figure 6) whereas the second and third diffusion models presented in Figure 7 expect a change of about 10%. These models are based on the behavior of iron that may not require a local reorganization during redox changes. Since change in cerium local structure doesn't have time to occur during the quench, the change in redox state expected by the models doesn't occur, explaining its absence in Figure 6.

Another observation can be made concerning the optical absorption spectra presented in figure 4.D, where two different contributions are needed in order to fit Ce(IV)-OMCT. Even though this is common in literature[31,32], this implies two different Ce(IV)-O distances in the glass. This could be explained by the presence of two distinct local structures or a distorted site, though we have found no further evidence supporting any of these hypotheses.

4.6. Raman assessment of cerium redox state. As discussed in section 4.4, Raman spectroscopy is sensitive to both cerium concentration and redox state. Moreover, Figure 9.B shows that is it possible to link the equilibrium temperature of a cerium containing glass to the Raman

spectra. Since the redox state at room temperature is representative of the equilibrium state from which it is quenched, it is possible to use the data obtained by *in situ* XANES spectroscopy to convert the temperature shown in Figure 9.B to Ce(IV) concentration. The results are presented in Figure 10 below.

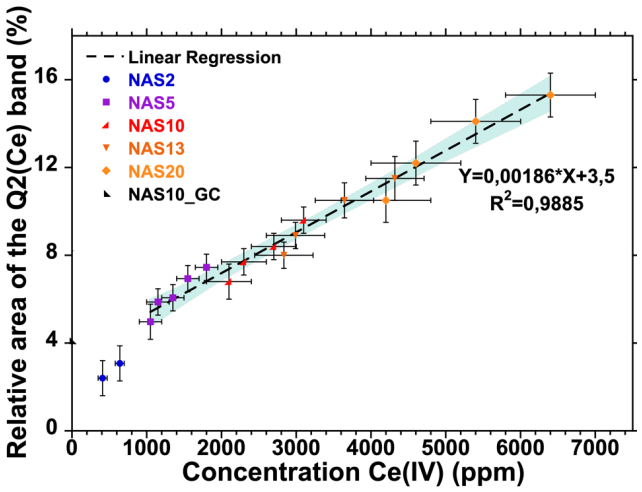

Figure 10. Evolution of the relative area of the Q^2(Ce) band with increasing Ce(IV) concentration determined using XANES data. Each symbol corresponds to a different total Ce concentration. Linear regression is performed on the NAS5 to NAS20 sample. Blue background corresponds to the 99% confidence interval given by linear regression.

For concentrations ranging from 5 to 20 mol‰ CeO_2, a linear trend is observed. Although each sample seems to follow a different linear relationship, a single equation fits well in the studied range.

The NAS2 sample is clearly off trend, even considering the 99% confidence limit. One could believe that the small contribution of the Q^2(Ce) band makes the deconvolution unreliable. Extrapolating the linear fit to the NAS2 sample equilibrated at 1600°C (lowest Ce(IV) concentration for the NAS2 series) gives a predicted value of 4.3%, very close to the value measured for the NAS5 sample equilibrated at 1600°C (of 5.1%). However, despite the similar Ce(IV) concentrations, the Raman spectra of these two glasses are distinctly different (Figure 3) and thus the behavior observed for the NAS2 sample in figure 10 cannot be solely due to the deconvolution procedure. We hypothesize that a linear model cannot be extended to very dilute CeO_2 concentrations, as other phenomena might be present at these concentrations.

Using the calibration in Figure 10 and knowing the total amount of cerium in the sample, it is possible to determine Ce redox state using Raman spectroscopy. This could allow for a fast assessment of cerium redox state in glasses with minimal sample preparation. However, since Raman spectroscopy is very sensitive to glass structure, it is likely necessary to reestablish this calibration curve when changing glass composition.

4. Conclusion:

XANES, wet chemistry and Raman spectroscopy reveal that cerium redox state in sodium aluminosilicate glasses is out of equilibrium and is representative of a high temperature redox state. It is therefore necessary to control oxido-reduction processes in the melt to better tune redox properties of the final products. The temperature of synthesis is therefore of paramount importance and should not be overlooked when comparing different samples or studies. Both the enthalpy and the entropy of reduction were measured using *in situ* XANES spectroscopy. As long as redox equilibrium was reached, it is possible to predict cerium redox state at different temperature, under different atmospheres, as well as at room temperature.

Optical absorption spectroscopy is also able to measure the redox state of cerium though the values obtained do not correspond to those from XANES or wet chemistry methods. This discrepancy is in part due to the iron contamination in our samples. However, this technique seems promising for the study of cerium in very dilute conditions, as the absorption of both trivalent and tetravalent cerium are intense.

Upon addition of cerium oxide to a sodium aluminosilicate glass, an additional contribution is visible in the Raman spectra, associated with the apparition of Q^2 units at least partially compensated by tetravalent and/or trivalent cerium. This vibration is redox sensitive as it is enhanced upon oxidation of the sample. This highlights Raman spectroscopy a viable tool to assess both cerium concentration and redox state in the glass, as a simple linear fit between the relative area of the Q^2(Ce) band and the concentration of tetravalent cerium allows determination of cerium redox state.

Supplementary Material

Optical absorption spectra of NAS2, NAS2H2 and NAS20 samples. VV and VH polarized Raman decomposition of the NAS2, NAS5, NAS13 and NAS20 samples. Example of cerium photo-oxidation over time recorded for NAS0.4 on the LUCIA beamline (SOLEIL) and for NAS10 on the ODE beamline (SOLEIL). Example of CeO_2 crystallization, Raman spectroscopy and optical microscopy. Complementary table of the decomposition parameters: Supplementary Figures S.1 to S.5. and Supplementary Table S.I (PDF).

Acknowledgments

We thank SOLEIL (Gif-sur-Yvette, France) for provision of synchrotron facilities (project numbers 20221616 and 20220496) as well as Lucie Nataf and Nicolas Trcera for their help on the ODE and Lucia beamline respectively. We thank Sandrine Brecy, Damien Lenord and Jérôme Dilscher from the Corning European Technology Center for their help with the experiments as well as Monique Comte for initiating the project. We thank Anatoly

Arkhipin and Alexander Pisch for their help on the LUCIA beamline. We thank Randall E. Youngman for his valuable assistance during the manuscript writing stage.
This work was supported by ANRT, under the CIFRE Contract 2021/0986 and by Corning SAS.

Author declarations section

Conflict of interest

The authors have no conflict of interest to disclose.

Author contributions

Adrien Donatini: Investigation (lead); Visualization (lead); Writing/Original draft preparation (lead); Writing/Review & Editing (equal). **Peggy Georges:** Funding Acquisition (lead); Conceptualization (equal); Resources (equal); Supervision (equal); Writing/Review & Editing (equal). **Tiphaine Fevre:** Conceptualization (equal); Supervision (equal); Writing/Review & Editing (equal). **Laurent Cormier:** Conceptualization (equal); Resources (equal); Supervision (equal); Writing/Original draft preparation (supporting); Writing/Review & Editing (equal). **Daniel Neuville:** Conceptualization (equal); Resources (equal); Supervision (equal); Writing/Review & Editing (equal).

Data availability statement

The data that support the findings of this study are available from the corresponding author upon reasonable request.

REFERENCES

(1) Jetschke, S.; Unger, S.; Schwuchow, A.; Leich, M.; Jäger, M. Role of Ce in Yb/Al Laser Fibers: Prevention of Photodarkening and Thermal Effects. *Opt. Express* **2016**, *24* (12), 13009. https://doi.org/10.1364/OE.24.013009.

(2) Engholm, M.; Jelger, P.; Laurell, F.; Norin, L. Improved Photodarkening Resistivity in Ytterbium-Doped Fiber Lasers by Cerium Codoping. *Opt. Lett.* **2009**, *34* (8), 1285. https://doi.org/10.1364/OL.34.001285.

(3) Liu, X.; Liu, C.; Chen, G.; Li, H. Influence of Cerium Ions on Thermal Bleaching of Photo-Darkened Ytterbium-Doped Fibers. *Front. Optoelectron.* **2018**, *11* (4), 394–399. https://doi.org/10.1007/s12200-018-0832-y.

(4) Yılmaz, D.; Aktaş, B.; Yalçın, Ş.; Albaşkara, M. Erbium Oxide and Cerium Oxide-Doped Borosilicate Glasses as Radiation Shielding Material. *Radiation Effects and Defects in Solids* **2020**, *175* (5–6), 458–471. https://doi.org/10.1080/10420150.2019.1674301.

(5) Wang, Z.; Cheng, L. Structural Evolution of CeO_2 -Doped Alkali Boroaluminosilicate Glass and the Correlation with Physical Properties Based on a Revised Structural Parameter Analysis. *RSC Adv.* **2016**, *6* (7), 5456–5465. https://doi.org/10.1039/C5RA20487A.

(6) Kamonpha, P.; Manyum, P.; Chanthima, N.; Tariwong, Y.; Triamnak, N.; Yimnirun, R.; Rujirawat, S.; Kidkhunthod, P.; Kothan, S.; Kim, H. J.; Kaewkhao, J. Structural and Luminescence Investigation of Ce^{3+} Doped Lithium Barium Gadolinium Phosphate Glass Scintillator. *Radiation Physics and Chemistry* **2021**, *185*, 109488. https://doi.org/10.1016/j.radphyschem.2021.109488.

(7) Ronda, C.; Wieczorek, H.; Khanin, V.; Rodnyi, P. Review—Scintillators for Medical Imaging: A Tutorial Overview. *ECS Journal of Solid State Science and Technology* **2016**, *5*, R3121–R3125. https://doi.org/10.1149/2.0131601jss.

(8) Kielty, M. W. Cerium Doped Glasses: Search for a New Scintillator. MSc Thesis. *TigerPrints Clemson University* **2016**. https://tigerprints.clemson.edu/all_theses/2545.

(9) Teng, L.; Jiang, Y.; Zhang, W.; Wei, R.; Guo, H. Highly Transparent Cerium Doped Glasses with Full-band UV-shielding Capacity. *Journal of the American Ceramic Society* **2020**, *103* (5), 3249–3256. https://doi.org/10.1111/jace.17020.

(10) Jiang, Y.; Wang, L.; Zhang, W.; Teng, L.; Hu, F.; Guo, H. Dual-Valence Ce Doped UV-Shielding Glasses with High Transparency and Stability. *Ceramics International* **2020**, *46* (10), 16032–16037. https://doi.org/10.1016/j.ceramint.2020.03.153.

(11) Stroud, J. S. Color Centers in a Cerium-Containing Silicate Glass. *The Journal of Chemical Physics* **1962**, *37* (4), 836–841. https://doi.org/10.1063/1.1733170.

(12) Stroud, J. S. Photoionization of Ce^{3+} in Glass. *The Journal of Chemical Physics* **1961**, *35* (3), 844–850. https://doi.org/10.1063/1.1701227.

(13) Weber, M. J.; Bliss, M.; Craig, R. A.; Sunberg, D. S. Scintillators and Applications: Cerium-Doped Materials. *Radiation Effects and Defects in Solids* **1995**, *134* (1–4), 23–29. https://doi.org/10.1080/10420159508227178.

(14) Hujova, M. Influence of Fining Agents on Glass Melting: A review, Part 1. *Ceramics - Silikaty* **2017**, 119–126. https://doi.org/10.13168/cs.2017.0006.

(15) Dejkena, M., J; Gomez, S. Fining Agents for Silicate Glasses. EP 2 535 320 A2, December 19, **2012**.

(16) Pereira, L.; Podda, O.; Fayard, B.; Laplace, A.; Pigeonneau, F. Experimental Study of Bubble Formation in a Glass-Forming Liquid Doped with Cerium Oxide. *Journal of the American Ceramic Society* **2020**, *103* (4), 2453–2462. https://doi.org/10.1111/jace.16950.

(17) Rüssel, C.; von der Gönna, G. The Electrochemical Series of Elements in the Na_2O-$2SiO_2$ Glass Melt. *J. Non-Cryst. Solids* **1999**, No. 260, 147–154. https://doi.org/10.1016/S0022-3093(99)00563-3.

(18) Pinet, O.; Phalippou, J.; Di Nardo, C. Modeling the Redox Equilibrium of the Ce^{4+}/Ce^{3+} Couple in Silicate Glass by Voltammetry. *J. Non-Cryst. Solids* **2006**, *352* (50–51), 5382–5390. https://doi.org/10.1016/j.jnoncrysol.2006.08.034.

(19) Wiedenroth, A.; Rüssel, C. The Effect of MgO on the Thermodynamics of the Fe^{2+}/Fe^{3+}-Redox Equilibrium and the Incorporation of Iron in Soda-Magnesia-Aluminosilicate Melts. *J. Non-Cryst. Solids* **2003**, *320* (1), 238–245. https://doi.org/10.1016/S0022-3093(03)00076-0.

(20) Le Losq, C.; Moretti, R.; Oppenheimer, C.; Baudelet, F.; Neuville, D. R. In Situ XANES Study of the Influence of Varying Temperature and Oxygen Fugacity on Iron Oxidation State and Coordination in a Phonolitic Melt. *Contrib Mineral Petrol* **2020**, *175* (7), 64. https://doi.org/10.1007/s00410-020-01701-4.

(21) Tilquin, J.-Y.; Duveiller, P.; Glibert, J.; Claes, P. Effect of Basicity on Redox Equilibria in Sodium Silicate Melts: An in Situ Electrochemical Investigation. *J. Non-Cryst. Solids* **1997**, *211* (1–2), 95–104. https://doi.org/10.1016/S0022-3093(96)00616-3.

(22) Vercamer, V.; Lelong, G.; Hijiya, H.; Kondo, Y.; Galoisy, L.; Calas, G. Diluted Fe 3+ in Silicate Glasses: Structural Effects of Fe-Redox State and Matrix Composition. An Optical Absorption and X-Band/Q-Band EPR Study. *J. Non-Cryst. Solids* **2015**, *428*, 138–145. https://doi.org/10.1016/j.jnoncrysol.2015.08.010.

(23) Vantelon, D.; Trcera, N.; Roy, D.; Moreno, T.; Mailly, D.; Guilet, S.; Metchalkov, E.; Delmotte, F.; Lassalle, B.; Lagarde, P.; Flank, A.-M. The LUCIA Beamline at SOLEIL. *J Synchrotron Rad* **2016**, 23 (2), 635–640. https://doi.org/10.1107/S1600577516000746.

(24) Nataf, L.; Baudelet, F.; Polian, A.; Jonane, I.; Anspoks, A.; Kuzmin, A.; Irifune, T. Recent Progress in High Pressure X-Ray Absorption Spectroscopy Studies at the ODE Beamline. *High Pressure Research* **2020**, 40 (1), 82–87. https://doi.org/10.1080/08957959.2019.1700979.

(25) Neuville, D. R.; Mysen, B. O. Role of Aluminium in the Silicate Network: In Situ, High-Temperature Study of Glasses and Melts on the Join SiO_2-$NaAlO_2$. *Geochimica et Cosmochimica Acta* **1996**, *60* (10), 1727–1737. https://doi.org/10.1016/0016-7037(96)00049-X

(26) Newville, M. Larch: An Analysis Package for XAFS and Related Spectroscopies. *J. Phys.: Conf. Ser.* **2013**, *430*, 012007. https://doi.org/10.1088/1742-6596/430/1/012007.

(27) Wojdyr, M. Fityk: A General-Purpose Peak Fitting Program. *J Appl Cryst* **2010**, *43* (5), 1126–1128. https://doi.org/10.1107/S0021889810030499.

(28) Duffy, J. A. Optical Basicity: A Practical Acid-Base Theory for Oxides and Oxyanions. *J. Chem. Educ.* **1996**, *73* (12), 1138. https://doi.org/10.1021/ed073p1138.

(29) Burnham, A. D.; Berry, A. J. The Effect of Oxygen Fugacity, Melt Composition, Temperature and Pressure on the Oxidation State of Cerium in Silicate Melts. *Chemical Geology* **2014**, *366*, 52–60. https://doi.org/10.1016/j.chemgeo.2013.12.015.

(30) Schreiber, H. D.; Lauer, H. V.; Thanyasiri, T. Oxidation-Reduction Equilibria of Iron and Cerium in Silicate Glasses: Individual Redox Potentials and Mutual Interactions. *J. Non-Cryst. Solids* **1980**, *38–39*, 785–790. https://doi.org/10.1016/0022-3093(80)90532-3.

(31) Herrmann, A.; Othman, H. A.; Assadi, A. A.; Tiegel, M.; Kuhn, S.; Rüssel, C. Spectroscopic Properties of Cerium-Doped Aluminosilicate Glasses. *Opt. Mater. Express* **2015**, *5* (4), 720–732. https://doi.org/10.1364/OME.5.000720.

(32) Brandily-Anne, M.-L.; Lumeau, J.; Glebova, L.; Glebov, L. B. Specific Absorption Spectra of Cerium in Multicomponent Silicate Glasses. *J. Non-Cryst. Solids* **2010**, *356* (44), 2337–2343. https://doi.org/10.1016/j.jnoncrysol.2010.02.020.

(33) Rygel, J. L.; Chen, Y.; Pantano, C. G.; Shibata, T.; Du, J.; Kokou, L.; Woodman, R.; Belcher, J. Local Structure of Cerium in Aluminophosphate and Silicophosphate Glasses. *Journal of the American Ceramic Society* **2011**, *94* (8), 2442–2451. https://doi.org/10.1111/j.1551-2916.2011.04596.x.

(34) Zaman, M. M.; Antao, S. M. Crystal Structure Refinements of Four Monazite Samples from Different Localities. *Minerals* **2020**, *10* (11), 1028. https://doi.org/10.3390/min10111028.

(35) Schreiber, H. D. Redox Processes in Glass-Forming Melts. *J. Non-Cryst. Solids* **1986**, *84* (1–3), 129–141. https://doi.org/10.1016/0022-3093(86)90770-2.

(36) Cachia, J.-N.; Deschanels, X.; Den Auwer, C.; Pinet, O.; Phalippou, J.; Hennig, C.; Scheinost, A. Enhancing Cerium and Plutonium Solubility by Reduction in Borosilicate Glass. *Journal of Nuclear Materials* **2006**, *352* (1–3), 182–189. https://doi.org/10.1016/j.jnucmat.2006.02.052.

(37) Smythe, D. J.; Brenan, J. M. Cerium Oxidation State in Silicate Melts: Combined fO_2, Temperature and Compositional Effects. *Geochimica et Cosmochimica Acta* **2015**, *170*, 173–187. https://doi.org/10.1016/j.gca.2015.07.016.

(38) Smythe, D. J.; Brenan, J. M.; Bennett, N. R.; Regier, T.; Henderson, G. S. Quantitative Determination of Cerium Oxidation States in Alkali-Aluminosilicate Glasses Using M4,5-Edge XANES. *J. Non-Cryst. Solids* **2013**, *378*, 258–264. https://doi.org/10.1016/j.jnoncrysol.2013.07.017.

(39) Le Losq, C.; Neuville, D. R.; Florian, P.; Henderson, G. S.; Massiot, D. The Role of Al^{3+} on Rheology and Structural Changes in Sodium Silicate and Aluminosilicate Glasses and Melts. *Geochimica et Cosmochimica Acta* **2014**, *126*, 495–517. https://doi.org/10.1016/j.gca.2013.11.010.

(40) McMillan, P. Structural Studies of Silicate Glasses and Melts-Applications and Limitations of Raman Spectroscopy. *American Mineralogist* **1984**, *69*, 622–644.

(41) Virgo, D.; Mysen, B. O.; Kushiro, I. Anionic Constitution of 1-Atmosphere Silicate Melts: Implications for the Structure of Igneous Melts. *Science* **1980**, *208* (4450), 1371–1373. https://doi.org/10.1126/science.208.4450.1371.

(42) Yadav, A. K.; Singh, P. A Review of the Structures of Oxide Glasses by Raman Spectroscopy. *RSC Adv.* **2015**, *5* (83), 67583–67609. https://doi.org/10.1039/C5RA13043C.

(43) Seifert, F.; Mysen, B. O.; Virgo, D. Three-Dimensional Network Structure of Quenched Melts (Glass) in the Systems SiO_2-$NaAlO_2$, SiO_2-$CaAl_2O_3$ and SiO_2-$MgAl_2O_3$. *American Mineralogist* **1982**, *67*, 696–717.

(44) Sarnthein, J.; Pasquarello, A.; Car, R. Origin of the High-Frequency Doublet in the Vibrational Spectrum of Vitreous SiO_2. *Science* **1997**, *275* (5308), 1925–1927. https://doi.org/10.1126/science.275.5308.1925.

(45) Pasquarello, A.; Sarnthein, J.; Car, R. Dynamic Structure Factor of Vitreous Silica from First Principles: Comparison to Neutron-Inelastic-Scattering Experiments. *Phys. Rev. B* **1998**, *57* (22), 14133–14140. https://doi.org/10.1103/PhysRevB.57.14133.

(46) Tuschel, D. Practical Group Theory and Raman Spectroscopy, Part II: Application of Polarization. *Spectroscopy* **2014**, *29*, 14.

(47) Czernuszewicz, R. S.; Spiro, T. G. IR, Raman, and Resonance Raman Spectroscopy. In *Inorganic Electronic Structure and Spectroscopy, Volume I*; Solomon, E. I., Lever, A. B. P., Eds.; Wiley, 2006; pp 368–379.

(48) McMillan, P. A Raman Spectroscopic Study of Glasses in the System CaO-MgO-SiO_2. *American Mineralogist* **1984**, *69*, 645–659.

(49) McMillan, P. F.; Piriou, B. Raman Spectroscopic Studies of Silicate and Related Glass Structure : A Review. *Bulletin de Minéralogie* **1983**, *106* (1), 57–75. https://doi.org/10.3406/bulmi.1983.7668.

(50) Piriou, B. The High-Frequency Vibrational Spectra of Vitreous and Crystalline Orthosilicates. *American Mineralogist* **1983**, *68*, 426–443.

(51) Magnien, V.; Neuville, D. R.; Cormier, L.; Roux, J.; Hazemann, J.-L.; Pinet, O.; Richet, P. Kinetics of Iron Redox Reactions in Silicate Liquids: A High-Temperature X-Ray Absorption and Raman Spectroscopy Study. *Journal of Nuclear Materials* **2006**, *352* (1), 190–195. https://doi.org/10.1016/j.jnucmat.2006.02.053.

(52) Magnien, V.; Neuville, D. R.; Cormier, L.; Roux, J.; Hazemann, J.-L.; De Ligny, D.; Pascarelli, S.; Pinet, O.; Richet, P.; Vickridge, I. Kinetics and Mechanisms of Iron Redox Reactions in Silicate Melts: The Effects of Temperature and Alkali Cations. *Geochimica et Cosmochimica Acta* **2008**, *72*, 2157–2168. https://doi.org/10.1016/j.gca.2008.02.007.

(53) Moretti, R. Polymerisation, Basicity, Oxidation State and Their Role in Ionic Modelling of Silicate Melts. *Annals of Geophysics* **2005**, *48* (4–5). https://doi.org/10.4401/ag-3221.

(54) Moretti, R. Ionic Syntax and Equilibrium Approach to Redox Exchanges in Melts: Basic Concepts and the Case of Iron and Sulfur in Degassing Magmas. In *Geophysical Monograph Series*; Moretti, R., Neuville, D. R., Eds.; Wiley, **2021**; pp 115–138. https://doi.org/10.1002/9781119473206.ch6.

(55) Johnston, W. D. Oxidation-Reduction Equilibria in Molten $Na_2O.2SiO_2$ Glass. *Journal of the American Ceramic Society* **1965**, *48* (4), 184–190. https://doi.org/10.1111/j.1151-2916.1965.tb14709.x.

(56) Paul, A. Effect of Thermal Stabilization on Redox Equilibria and Colour of Glass. *J. Non-Cryst. Solids* **1985**, *71* (1–3), 269–278. https://doi.org/10.1016/0022-3093(85)90296-0.

(57) Cooper, R. F. The Mechanism of Oxidation of a Basaltic Glass: Chemical Diffusion of Network-Modifying Cations. *Geochimica et Cosmochimica Acta* **1996**, *60* (17), 3253–3265.

(58) Cook, G. B.; Cooper, R. F.; Wu, T. Chemical Diffusion and Crystalline Nucleation during Oxidation of Ferrous Iron-Bearing Magnesium Aluminosilicate Glass. *J. Non-Cryst. Solids* **1990**, *120* (1), 207–222. https://doi.org/10.1016/0022-3093(90)90205-Z.

(59) Kress, V. C.; Carmichael, I. S. E. The Compressibility of Silicate Liquids Containing Fe203 and the Effect of Composition, Temperature, Oxygen Fugacity and Pressure on Their Redox States. *Contributions to*

Mineralogy and Petrology **1991** *108*, 82–92. https://doi.org/10.1007/BF00307328.

(60) Berry, A. J.; Shelley, J. M. G.; Foran, G. J.; O'Neill, H. St. C.; Scott, D. R. A Furnace Design for XANES Spectroscopy of Silicate Melts under Controlled Oxygen Fugacities and Temperatures to 1773 K. *J Synchrotron Rad* **2003**, *10* (4), 332–336. https://doi.org/10.1107/S0909049503007556.

(61) Schaller, T.; Stebbins, J. F.; Wilding, M. C. Cation Clustering and Formation of Free Oxide Ions in Sodium and Potassium Lanthanum Silicate Glasses: Nuclear Magnetic Resonance and Raman Spectroscopic Findings. *J. Non-Cryst. Solids* **1999**, *243*, 146–157. https://doi.org/10.1016/S0022-3093(98)00838-2.

(62) Ellison, A. J. G.; Hess, P. C. Lanthanides in Silicate Glasses: A Vibrational Spectroscopic Study. *Journal of Geophysical Research: Solid Earth* **1990**, *95* (B10), 15717–15726. https://doi.org/10.1029/JB095iB10p15717.

(63) Ellison, A. J. G.; Hess, P. C. Vibrational Spectra of High-Silica Glasses of the System K_2O-SiO_2-La_2O_3. *J. Non-Cryst. Solids* **1991**, *127*, 247–258. https://doi.org/10.1016/0022-3093(91)90477-N.

(64) Wang, Z.; Zhao, Z.; Peng, B.; Liu, D.; Xu, H.; Chen, Y.; Wang, D.; Liu, H.; Peng, N. Investigation on the Mechanism of the Immobilization of CeO_2 by Using Cullet-Based Glass (CBG). *Annals of Nuclear Energy* **2019**, *133*, 209–215. https://doi.org/10.1016/j.anucene.2019.05.027.

(65) Arai, K.; Namikawa, H.; Kumata, K.; Honda, T.; Ishii, Y.; Handa, T. Aluminum or Phosphorus Co-doping Effects on the Fluorescence and Structural Properties of Neodymium-doped Silica Glass. *Journal of Applied Physics* **1986**, *59* (10), 3430–3436. https://doi.org/10.1063/1.336810.

(66) Kiritchenko, N. V.; Kotov, L. V.; Melkumov, M. A.; Likhachev, M. E.; Bubnov, M. M.; Yashkov, M. V.; Laptev, A. Y.; Guryanov, A. N. Effect of Ytterbium Co-Doping on Erbium Clustering in Silica-Doped Glass. *Laser Phys.* **2015**, *25* (2), 025102. https://doi.org/10.1088/1054-660X/25/2/025102.

(67) Ishii, Y.; Arai, K.; Namikawa, H.; Tanaka, M.; Negishi, A.; Handa, T. Preparation of Cerium-Activated Silica Glasses: Phosphorus and Aluminum Codoping Effects on Absorption and Fluorescence Properties. *Journal of the American Ceramic Society* **1987**, *70* (2), 72–77. https://doi.org/10.1111/j.1151-2916.1987.tb04932.x.

(68) Shimizu, F.; Tokunaga, H.; Saito, N.; Nakashima, K. Viscosity and Surface Tension Measurements of RE_2O_3-MgO-SiO_2 (RE=Y, Gd, Nd and La) Melts. *ISIJ International* **2006**, *46* (3), 388–393. https://doi.org/10.2355/isijinternational.46.388.

(69) Aboelwafa, M. A.; Meikhail, M. S.; Oraby, A. H.; Abdelghany, A. M. Influence of Cerium Oxide on the Structural Aspects of Soda-Lime Aluminosilicate Glasses Synthesized by Sol-Gel Route. *Materials Chemistry and Physics* **2023**, *305*, 127930. https://doi.org/10.1016/j.matchemphys.2023.127930.

(70) Qi, J.; Liu, C.; Zhang, C.; Jiang, M. Effect of Ce_2O_3 on Structure, Viscosity, and Crystalline Phase of CaO-Al_2O_3-Li_2O-Ce_2O_3 Slags. *Metall Mater Trans B* **2017**, *48* (1), 11–16. https://doi.org/10.1007/s11663-016-0850-3.

(71) Czernuszewicz, R. S.; Zaczek, M. B. Resonance Raman Spectroscopy. In *Encyclopedia of Inorganic and Bioinorganic Chemistry*; Scott, R. A., Ed.; John Wiley & Sons, Ltd: Chichester, UK, 2011; p eibc0303. https://doi.org/10.1002/9781119951438.eibc0303.

(72) Clark, R. J. H.; Dines, T. J. Resonance Raman Spectroscopy, and Its Application to Inorganic Chemistry. New Analytical Methods (27). *Angew. Chem. Int. Ed. Engl.* **1986**, *25* (2), 131–158. https://doi.org/10.1002/anie.198601311.

(73) Wang, Z.; Cooney, T. F.; Sharma, S. K. In Situ Structural Investigation of Iron-Containing Silicate Liquids and Glasses. *Geochimica et Cosmochimica Acta* **1995**, *59* (8), 1571–1577. https://doi.org/10.1016/0016-7037(95)00063-6.